CHALMERS
UNIVERSITY OF TECHNOLOGY

Influence of Energy Density on the Anisotropy of Multi-Property Behaviour in Additively Manufactured Fe-Si Alloys

Master's thesis in Production Engineering

GOKUL BABU

DEPARTMENT OF INDUSTRIAL AND MATERIAL SCIENCE

CHALMERS UNIVERSITY OF TECHNOLOGY
Gothenburg, Sweden 2025
www.chalmers.se

Master's thesis 2025

Influence of Energy Density on the Anisotropy of Multi-Property Behaviour in Additively Manufactured Fe-Si Alloys

Additive Manufacturing and Characterization

GOKUL BABU

CHALMERS
UNIVERSITY OF TECHNOLOGY

Department of Industrial and Material Science
Chalmers University of Technology
Gothenburg, Sweden 2025

Influence of Energy Density on the Anisotropy of Multi-Property Behaviour in Additively Manufactured Fe-Si Alloys
GOKUL BABU

Supervisor: Dr Varun Chaudhary, Industrial and Materials Science
Examiner: Dr Varun Chaudhary, Industrial and Materials Science

Master's Thesis 2025
Department of Industrial and Materials Science
Chalmers University of Technology
SE-412 96 Gothenburg
Telephone +46 31 772 1000

Typeset in LaTeX
Printed by Chalmers Reproservice
Gothenburg, Sweden 2025

GOKUL BABU
Department of Industrial and Materials Science
Chalmers University of Technology

Abstract

The influence of volumetric energy density (VED) on the anisotropic magnetic, mechanical, and electrical properties of Fe–6.5 wt.% Si alloys fabricated by Powder Bed Fusion–Laser (PBF-L) was investigated. Laser power and scan speed were systematically varied while keeping other process parameters constant. Characterization by VSM, XRD, Vickers hardness (HV), electrical resistivity, and optical microscopy revealed pronounced anisotropy between the X–Z and X–Y planes. Samples produced at optimal VED showed higher saturation magnetization (M_s) and lower coercivity (H_c) along the build direction (BD), while variations in hardness and resistivity reflected the combined effects of residual stress and solidification dynamics. Optimizing VED effectively controls anisotropy in the multi-property response of PBF-L-processed Fe–6.5 wt.% Si, providing insights into process parameters for fabricating high-performance magnetic components for electric machine applications.

Keywords: Additive Manufacturing, PBF-L, VED, Fe–Si Alloys, Anisotropy, Magnetic Properties, Mechanical Properties, Electrical Resistivity.

Acknowledgements

I would like to express my deepest gratitude to my supervisor, Dr. Varun Chaudhary, for his exceptional guidance, encouragement, and unwavering support throughout the course of this thesis. His expertise and constructive feedback have been invaluable in shaping the direction and quality of this work. I would also like to extend my sincere appreciation to Mr. Mukesh Murali for his valuable advice, technical assistance, and continuous support during the project.

I sincerely thank Chalmers University of Technology and the Department of Industrial and Materials Science for providing me with the opportunity, resources, and a conducive research environment to undertake this study.

Gokul Babu, Gothenburg, 10 2025

List of Acronyms

Below is the list of acronyms that have been used throughout this thesis listed in alphabetical order:

AM	Additive Manufacturing
BD	Build Direction
TD	Transverse Direction
SD	Standard Deviation
PBF-L	Powder Bed Fusion – Laser
VED	Volumetric Energy Density
LED	Linear Energy Density
VSM	Vibrating Sample Magnetometer
XRD	X-Ray Diffraction
OM	Optical Microscopy
HV	Vickers Hardness
Ms	Saturation Magnetization
Hc	Coercivity
ρ	Electrical Resistivity
P	Laser Power (W)
v	Scan Speed (mm/s)
h	Hatch Spacing (mm)
t	Layer Thickness (mm)
σ	Applied Mechanical Stress (MPa)
ε	Strain
d	Grain Size (μm)
N	Number of Indents (for Hardness Test)
Mr	Remanent Magnetization (emu/g)
μ	Magnetic Permeability (H/m)
H_K	Magnetic Anisotropy Field (A/m)
K_1	First-Order Magnetocrystalline Anisotropy Constant (J/m^3)
λ_s	Saturation Magnetostriction Constant
θ	Angle between Stress and Magnetization (degrees)
J	Current Density (A/m^2)
E	Electric Field (V/m)
r	Pearson Correlation

Nomenclature

Below is the nomenclature of indices, parameters, and variables that have been used throughout this thesis.

Indices

BD	Build Direction
TD	Transverse Direction
XY	Plane perpendicular to BD
XZ	Plane parallel to BD

Parameters

P	Laser power (W)
V	Scan speed (mm/s)
h	Hatch spacing (mm)
t	Layer thickness (mm)
VED	Volumetric energy density = $\frac{P}{v \cdot h \cdot t}$ (J/mm^3)
LED	Linear energy density (J/mm)
HV	Vickers hardness
σ	Applied mechanical stress (MPa)
ε	Strain
d	Average grain size (μm)
N	Number of indents
μ	Magnetic permeability (H/m)
μ_0	Permeability of free space ($4\pi \times 10^{-7}$ H/m)
K_1	First-order magnetocrystalline anisotropy constant (J/m^3)
λ_s	Saturation magnetostriction constant
θ	Angle between stress and magnetization (°)
ρ	Electrical resistivity ($\mu\Omega$·cm)

Variables

M_s	Saturation magnetization (emu/g)
M_r	Remanent magnetization (emu/g)

H_c	Coercivity (Oe)
$\vec{H}$	Magnetic field intensity (A/m)
$\vec{B}$	Magnetic flux density (T)
$\vec{M}$	Magnetization vector (A/m)
H_K	Magnetic anisotropy field (A/m)
J	Current density (A/m^2)
E	Electric field (V/m)
ΔT	Temperature gradient between layers (K)
R.D.	Relative density (%)

Contents

List of Figures

List of Tables

1

Introduction

1.1 Background

The United Nations Sustainable Development ambition of reducing CO_2 emissions by 2030 has accelerated the search for alternative fuel sources by several countries[9]. The key approach of several countries is to reduce sources of emissions, primarily from transportation and factories, which leads to an increased demand for magnetic materials in high-performance applications. Soft magnetic materials are characterized by high permeability (μ), low H_c, and minimal hysteresis losses, suitable for electromechanical energy systems. Thus increasing the efficiency of devices such as electric motors, transformers, and inductors operating under high magnetic fields.

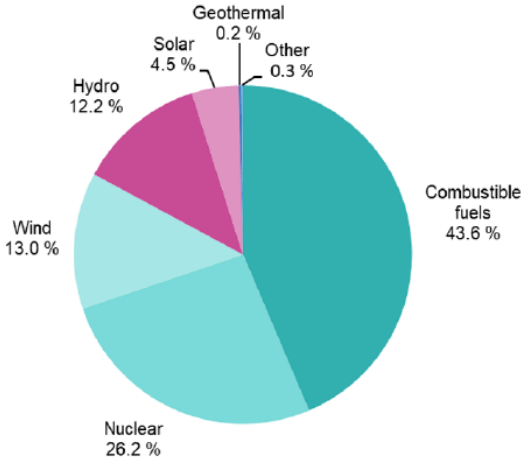

Figure 1.1: The primary sources of energy for the EU in GWh (2019) [1].

According to [1], the demand for electric motors is expected to increase due to their significant role in energy conversion across various sources, as illustrated in Figure 1.1. The silicon steels (3.2 wt % Si) are widely used in industry with a market share of 80% globally, around 10 million tons annually worldwide [10]. The Fe–3.2 wt % Si are primarily used in mass production of heavy-duty flux multipliers in the core of transformers, motors, etc due to their equally enhanced electrical and magnetic properties at a lower cost[11]. Traditionally magnetic materials are operated in the frequency of 50/60 Hz. However, there is a need for devices to operate at higher excitation frequencies (by non-sinusoidal waveforms) without increased core loss, where the magnetic field alternates at variable speed and frequency operations [12].

The alloys currently used are grain-oriented silicon steel (GOES), typically Fe–3 %Si in transformers and non-oriented silicon steel in electrical motor, usually suffer from increased core losses and magnetostriction-induced noise, limiting their performance in next-generation applications [6, 10].

A viable alternative is Fe–6.5 wt.% Si due to its high ρ and producing near-zero magnetostriction in both $\langle 1\ 0\ 0 \rangle$ and $\langle 1\ 1\ 1 \rangle$ axes combined, resulting in smoother operation without much humming noise and vibrations[10]. The addition of silicon causes the alloy to become more brittle due to the formation of ordered phases (B2 and DO3 phases). Thus, limiting the manufacturability of Fe–6.5 wt% Si material using conventional methods such as cold rolling process[10, 6]. Additive manufacturing (AM) can be used to overcome this limitations, especially the PBF-L process represents a possible way to produce parts of complex shapes with minimal mechanical deformation [1]. In PBF-L, one of the critical macroparameters used is VED. VED directly governs the melt pool size, solidification rate, microstructure and crystallographic texture effectively enabling us to manipulate to fabricate the required component. The previous studies by [13] have shown that parts produced in PBF-L using Fe–6.5 wt% Si material, the mechanical, magnetic, and electrical properties vary drastically with BD of the part. For electric motor applications, this anisotropy can result in non-uniform magnetic distribution, torque ripples, high noise, and lower efficiency.

1.2 Aim and Objectives

Investigating Fe–6.5 wt% Si alloys offers significant potential for developing materials suited to extreme thermal environments, such as those encountered in automotive and aerospace applications. This study focuses on optimizing the PBF-L process parameters, particularly the VED, and examining their effects on the anisotropy of mechanical, electrical, and magnetic properties of Fe–6.5 wt% Si alloys. The specific objectives are to establish correlations between energy density, anisotropic microstructure, and the resulting variations in mechanical, magnetic, and electrical performance. Furthermore, the study aims to assess anisotropy in these properties in PBF-L fabricated Fe–6.5 wt% Si alloys, and to investigate how different VED levels influence the microstructure and crystallographic texture parallel and perpendicular to the BD.

1.3 Delimitation

In the context of AM, this study does not attempt to address all sources of anisotropy or processing variability. Instead, it is delimited to exploring how VED affects anisotropic microstructures and their resulting mechanical, electrical, and magnetic behaviours in Fe–6.5 wt% Si alloys. Broader issues such as cost-efficiency, large-scale manufacturability, and alternative AM techniques are outside the scope of this work.

2

Theoretical framework

2.1 Soft Magnetic Materials

Electromagnetic devices require materials with high μ, low H_c, and minimal core loss [6]. However, conventional manufacturing techniques often introduce defects and magnetic anisotropies [1]. Soft magnetic materials are particularly well-suited for such applications due to their capacity to be easily magnetized and demagnetized under low applied magnetic fields. As shown in the Figure 2.1, these materials typically exhibit H_c below 1000 A/m or 12.6 Oe, relative permeability (μ_r) in the range of 10^4 to 10^5 μ_r, low remanence (M_r), and high M_s [14]. The soft magnetic materials are primarily categorized into:

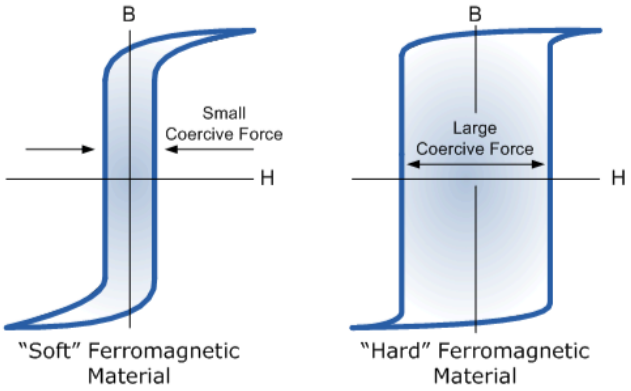

Figure 2.1: The B-H curve for soft and hard ferromagnetic material [2].

- **Fe–Si Alloys**: Fe–Si alloys, commonly known as silicon steels or electrical steels, with silicon concentration ranging from 2-7 Wt.% [6]. When the silicon content exceeds 4 Wt.%, the alloy becomes brittle due to the formation of ordered B_2 and DO_3 phases within the body-centred cubic (BCC) Iron lattice. Fe–Si alloys are categorized into two types, grain-oriented and non-oriented steels. Grain-oriented Fe-Si steels are processed to align the grains with the $\langle 100 \rangle$ crystallographic texture parallel to the rolling direction. Grain-oriented steels have high magnetic properties in the rolling direction and show anisotropic behaviour with other axes. The grain-oriented Fe–3 wt% Si alloys are widely used for transformer cores. Whereas the non-oriented steels have magnetic properties similar in all directions and are isotropic in nature, with the crystallographic orientation arranged randomly. The non-oriented steels are mostly used in electric motor cores[12].

- **Ni–Fe Alloys**: Ni–Fe alloys consists of 50 or 80% of nickel with iron and are also known as permalloy [6]. These alloys have exceptionally high initial permeabilities (104 μ_0), extremely low H_c (8 A/m), and higher ρ compared to Fe–Si alloys [11]. Another variant of permalloy known as supermalloy with the composition of $Ni_{79}Fe_{15}Mo_5Mn_{0.5}$ has the maximum μ_r of 10^6 and H_c of 0.16 A/m, the highest for ever produced material [11].
- **Amorphous Alloys and Nanocrystalline Alloys**: Amorphous alloys are typically based on iron or cobalt and are alloyed with metalloids such as boron, silicon for stabilization of the amorphous structure [11, 12]. These alloys are produced using melt spinning technique with a rapid solidification, with cooling rates of 10^6 k/s, which suppress the formation of a crystalline lattice [12, 6]. Due to the absence of grain boundaries, crystallographic texture, and irregular atomic arrangements, amorphous alloys exhibit low hysteresis and eddy current losses, making them ideal for high-frequency applications [12, 6]. Nanocrystalline alloys are derived from amorphous alloys through controlled annealing above crystallization temperatures[11]. The first produced nanocrystalline soft magnetic alloys consist of Fe–Si–B–Nb (niobium)–Cu[12]. They show magnetic properties similar to permalloy and also have high saturation induction (B_s) of 1.2 T [11].

2.2 Challenges in Conventional Manufacturing

The Fe-Si alloys with silicon less than 4.5wt% are traditionally manufactured using mechanical rolling. The Fe-3.2wt% Si is commonly used in transformers and electric motors due to their feasibility to mass produce and significantly lower cost compared to other Fe-Si alloys [15]. Also, it is unfeasible to produce Fe-Si alloys having a silicon percentage greater than 4.5wt.% due to their brittleness and technical constraints to achieve a thickness in the range of 0.30–0.60 mm. AM provides a solution to address this challenge, due to the layer-by-layer printing strategy, the ordered phases can be suppressed partially if the Fe-Si alloy is cooled at a faster rate [16].

The findings by [17] show that AM produced Fe-Si alloys with higher silicon percentage up to 6.7 Wt% have shown a significant increase in the magnetic properties, such as μ reaching 31000 µ, where conventionally produced Fe-3% wt Si sheets showed a μ of 3000 µ. Whereas, the actual power loss was similar to mechanically rolled Fe-3% wt Si alloy and not feasible for mass production. For AM to be considered as a viable alternative to conventional manufacturing, the eddy current/ power loss needs to be minimized significantly. The suitable processing parameter, with the laser energy input density, scanning speed, rotation angle, etc, needs to be determined for achieving the required performance [17].

2.3 Powder Bed Fusion – Laser (PBF-L)

PBF-L is a complex AM technique that fabricates components layer by layer by selectively melting metal powders using a focused, high-energy laser beam [1]. A 3D CAD model of the required part is first created in .STL format and then sliced using appropriate AM software to generate the laser scanning path via G-codes. During fabrication, a uniform layer of metal powder is spread across the build platform. The laser then selectively scans and melts the regions corresponding to the sliced CAD model. After each layer is completed, the build platform is lowered by one layer thickness, and a new powder layer is deposited using powder roller mechanism after the piston holding the powder stock moves up [18]. The build chamber is filled with inert gases such as argon, nitrogen to create a protective atmosphere for highly reactive materials [19]. Figure 2.2 shows the working parts involved in Powder Bed Fusion–Laser Beam.

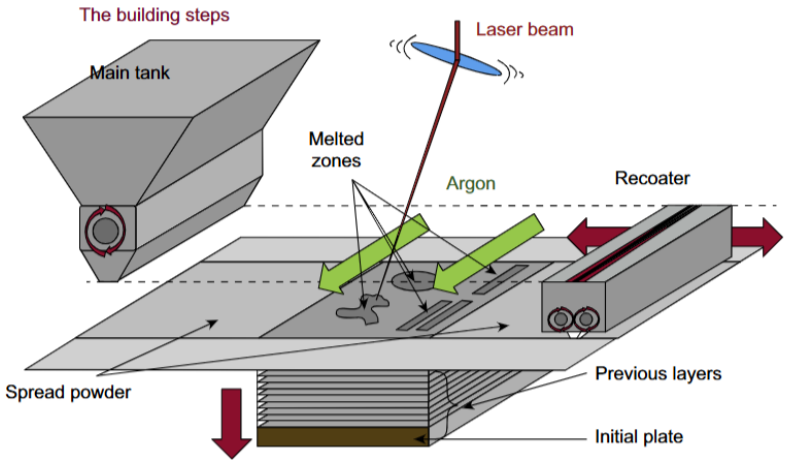

Figure 2.2: The schematic representation of PBF-L [3].

Fusion between successive layers occurs due to the combined effects of the Rayleigh length of the laser beam and thermal conduction from the underlying layer, and the process is repeated until the part is fully fabricated [18]. The quality of components produced by AM techniques such as PBF-L is determined by both powder characteristics and process parameters. The final properties of the component are strongly correlated with the feedstock and processing conditions, primarily due to the material's energy absorption behaviour and laser parameters, such as power density, which directly influence the thermal profile, solidification rate, and resulting microstructure [20]. Furthermore, process parameters, including laser power, scan speed, hatch distance, and layer thickness, play a critical role in minimizing defects by enabling the production of high-density parts with minimal porosity or voids. Achieving near-full density is a key objective in AM [21].

PBF-L offers transformative advantages for manufacturing Fe–6.5% Si components. The process eliminates the need for the conventional mechanical rolling process and

enables design freedom to produce complex and lightweight parts [10]. According to [17], the residual stresses increase with in height of the component in PBF-L and for Fe-Si alloys above 6 Wt.%, a maximum height of 10 mm can be built without much defects. Using a build-chamber pre-heating system for processing Fe–6.5 wt% Si samples reduces crack formation, allowing for greater design freedom with higher building height [17]. Also post post-processing activities such as heat treatment help in reducing the internal stresses.[8, 19].

2.4 Effects of Volumetric Energy Density

VED is defined as [8]:

$$VED = \frac{P}{v \cdot h \cdot t} (\mathrm{J/mm^3})$$

where P is the laser power, v is scan speed, h is hatch spacing, and t is the layer thickness. VED is a key process parameter in PBF-L, as it governs the melt pool geometry, cooling rate, and solidification behaviour. These factors directly influence grain morphology, microstructural evolution, and crystallographic texture [8].

At low VED values, the energy input is insufficient to fully melt the powder particles, leading to lack of fusion, porosity, and incomplete consolidation of layers. The resulting microstructure is defect-prone, with reduced mechanical strength and degraded magnetic performance [20].

Higher VED promotes formation of DO_3 ordered phases, increasing brittleness and reducing ductility due to restricted dislocation motion [22]. However, the lower VED leads to the formation of disordered α -Fe due to incomplete melting and higher cooling rate, which is soft, ductile, but has low magnetic properties. An optimal VED minimizes common AM defects such as porosity, balling, and hot tearing [22]. In contrast, excessively high VED values create unstable melt pools characterized by keyholing and excessive evaporation. These phenomena not only introduce defects but also accelerate the volatilization of silicon, which destabilizes the Fe–Si alloy composition. Furthermore, high VED promotes the formation of ordered B_2 and DO_3 phases, restricting dislocation motion and increasing brittleness.

At the other extreme, very low VED can favour rapid cooling and incomplete melting, stabilizing disordered α-Fe. Although this phase is soft and ductile, it exhibits poor magnetic properties, including reduced μ and M_s. Therefore, establishing an optimal VED window is essential. Balanced energy input minimizes common AM defects such as porosity, balling, and hot tearing, while also refining microstructure and suppressing detrimental ordered phases. This ensures that PBF-L processed Fe–6.5% Si alloys achieve both mechanical integrity and desirable magnetic performance.

2.5 Microstructural Anisotropy in AM

2.5.1 Origin of Anisotropy

In AM processes such as PBF-L, EBM, and DED, anisotropy originates from directional solidification under steep thermal gradients during layer-by-layer deposition [19]. This promotes elongated, columnar grains that grow epitaxially, producing highly textured microstructures and direction-dependent properties. This texture often favours specific crystallographic orientations such as ⟨001⟩ or ⟨011⟩ directions, depending on the alloy system [23]. Consequently, the mechanical, thermal, electrical, and magnetic properties of AM components become direction-dependent as shown in Figure 2.3 [20].

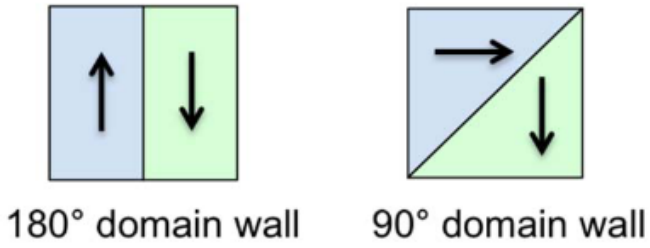

Figure 2.3: The schematic representation of 180° and 90° magnetic domain walls [4].

Mechanical properties are usually higher along the BD of the sample due to aligned grain boundaries and limited transverse grain intersections [20]. Similarly, directional dependencies are observed in thermal and electrical conductivity owing to reduced grain boundary scattering along the columnar grains [15]. Several factors influence the degree of anisotropy, including:

- Process parameters.
- Scanning strategies.
- Build orientation and geometry
- Thermal gradients and cooling rates.
- Alloy-specific nucleation and growth behaviour.

Phase-field simulations have confirmed that directional solidification under rapid cooling rates leads to persistent columnar microstructures [24]. To mitigate anisotropy, techniques such as preheating the building platform at a specific higher temperature, alloy modifications, and post-processing activities like Hot Isostatic Pressing (HIP) and heat treatment (HT) are being developed to relieve internal stresses, reduce defects, and promote grain growth [20, 19].

2.5.2 Magnetic anisotropy

Magnetic anisotropy refers to the variation in magnetic properties with different axes and positions in a material, influencing the magnetization behaviour. The magnetic anisotropy occurs due to both intrinsic and extrinsic factors. Intrinsic

factors correspond to the properties of the material itself, such as crystal structure and spin-orbit coupling. Extrinsic factors, on the other hand, correspond to the physical shape of the material and its interaction with the environment, such as its shape and stress [5, 6].

Magnetic anisotropy is a key parameter that distinguishes between soft and hard magnetic materials. Low anisotropy materials enable low H_c and low hysteresis, necessary for alternating magnetic fields. The anisotropy field, denoted H_K, is a fictitious or effective internal magnetic field used to represent the torque exerted by magnetic anisotropy. It is not a physically applied field but a conceptual tool used to model how strongly a material resists changes in magnetization direction [11, 5].

Formula

$$H_K = \frac{2K_1}{\mu_0 M_s} \quad [5]$$

Where:

- K_1: First-order magnetocrystalline anisotropy constant ($\mathrm{J/m^3}$)
- μ_0: Vacuum permeability ($4\pi \times 10^{-7}\,\mathrm{H/m}$)
- M_s: Saturation magnetization (A/m)

H_K quantifies the internal field strength required to rotate the magnetization away from the easy axis [5]. A higher H_K indicates a magnetically hard material, with greater resistance to demagnetization. It provides a theoretical upper bound for H_c, crucial for modelling magnetization reversal behaviour in materials and designing permanent magnets and high-anisotropy materials as shown in Figure 2.4. Provides insight into the stability of magnetic states under external fields [5, 11]. The magnetic anisotropy is influenced by the following:

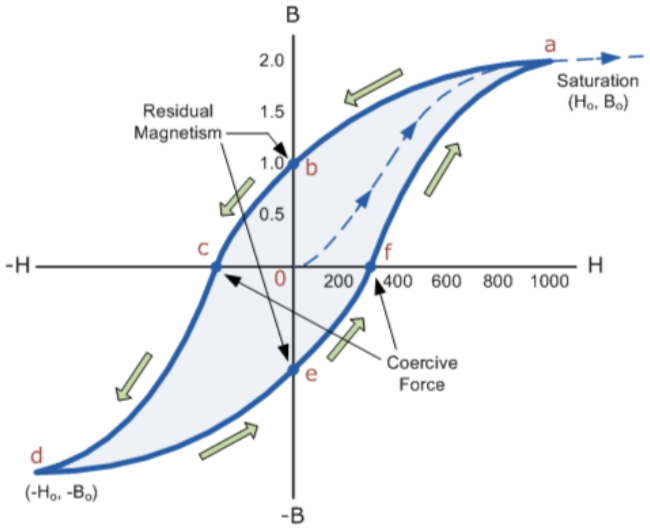

Figure 2.4: The representation of magnetic hysteresis loop for ferromagnetic material [2].

- **Magnetocrystalline Anisotropy**: It is defined as the material's magnetic properties that are directly proportional to the direction of magnetization relative to its crystal lattice, as shown in Figure 2.5 [5]. In BCC iron, magnetization occurs more readily along the ⟨100⟩ direction than the ⟨111⟩ direction [25]. Also, Fe-Si alloys with ordered phases such as DO_3 and B_2 exhibit strong magnetocrystalline anisotropy. This significantly influences the H_c, μ and hysteresis loss [10].

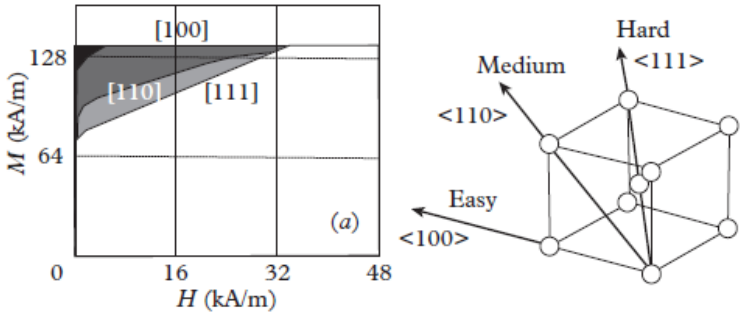

Figure 2.5: The M-H curve for Fe with field applied along three different crystallographic directions [5].

- **Shape or Magnetostatic Anisotropy**: It is the influence of a material's shape on the required direction of magnetization[5]. When an object is magnetized, magnetic poles form at its ends or surfaces. The magnetic fields created by these poles are called demagnetizing fields that resist the applied magnetizing field. Different shapes have different demagnetizing fields inside the material [14]. The preferred axis is the one with the lowest demagnetization factor. The effect of the demagnetizing field depends on the geometry. Materials having a long, thin shape have a weaker demagnetizing field along the length whereas flat, thin shapes have a strong demagnetizing field perpendicular to the plane. The magnetization is easier along the axis having weaker demagnetization field [6].
- **Magnetoelastic or Stress-Induced Anisotropy**: When a magnetic field is applied to a material as shown in Figure 2.6, there is a dimensional change in the length of the material, producing a strain called as magnetostriction [6]. When additional mechanical stress is applied to the substance, the coupling of mechanical stress and magnetostriction creates an easier and hard direction for magnetisation, known as stress-induced or Magnetoelastic anisotropy [5].

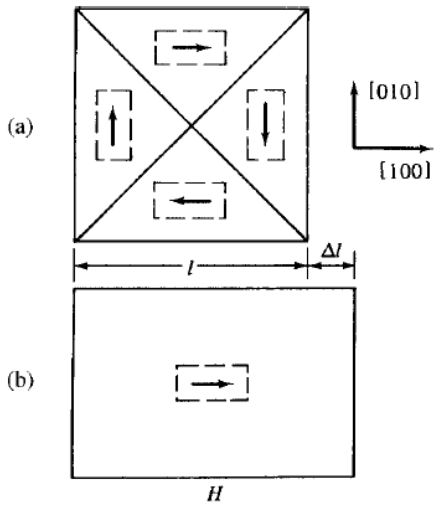

Figure 2.6: The magnetostriction in the [100] direction of an iron crystal [6]

2.5.3 Mechanical anisotropy

The mechanical properties can vary with different build orientation due to thermal gradients, cooling rates and phase transformation. The primary causes of mechanical anisotropy are:

- **Crystallographic Texture**: Mechanical properties such as strength, ductility, and hardness are highly dependent on the orientation of the grain. The grain structure often exhibits Goss texture 110<001> or Cube texture 100<001> during directional solidification in silicon steels [10]. Plastic deformation in crystalline materials occurs primarily through slip and twinning, with slip being the dominant mechanism in most materials. Depending on the orientation, slip systems can be suppressed and lead to brittle fracture, or slip systems can be activated and cause the material to be more ductile [17].
- **Dislocation Density**: Dislocations are the line defects in the crystal lattice, causing disruptions in the regular arrangement of atoms. Dislocation density is defined as the total length of dislocation lines present per unit volume. Higher dislocation densities typically strengthen materials by impeding plastic deformation [20].
- **Grain and Sub-grain Morphology**: The grain morphology refers to the shape, size, and orientation of individual crystalline grains in a polycrystalline material. The grains are classified as equiaxed grains, columnar grains, dendritic grains, sub-grains, and twinned. Based on the grain formed, such as equiaxed grains, columnar grains, the mechanical properties, such as ductility, yield strength, and hardness, significantly differ [20, 26].
- **Residual Stress**: Residual stress is the internal stress arising within the material when no load is applied. The stresses occur due to the non-uniform heating and cooling, phase transformation, thermal gradients and solidification cracking of the depositing layer [20].

2.5.4 Electrical anisotropy

Electrical anisotropy describes the variation in ρ or conductivity depending on the direction of current flow. In isotropic materials, ρ is the same in all directions. In anisotropic materials, ρ requires a tensor representation to assess the ρ present in different axis (x, y, z axis) [10]. The constitutive relation for electrical anisotropy is expressed as [12]:

$$\mathbf{E} = \boldsymbol{\rho} \cdot \mathbf{J}$$

where $\mathbf{E}$ is the electric field, $\mathbf{J}$ is the current density, and $\boldsymbol{\rho}$ is the resistivity tensor.

In Fe-Si alloys produced using PBF-L, electrical anisotropy arises from the material's internal structure. The layer-by-layer processing inherent to PBF-L generates thermal gradients that promote the growth of a preferred $\langle 001 \rangle$ crystallographic direction along the BD [27]. Electrical behaviour is also highly sensitive to residual stresses and defects, such as cracks or porosity, which contribute to anisotropy between different axes [10]. Furthermore, the formation of ordered phases (B2 and $D0_3$) introduces internal stresses and structural heterogeneity, further amplifying the directional dependence of electrical properties and increasing eddy current losses [10].

3
Research Methodology

3.1 Design of Experiments

Initially, 45 samples were fabricated with varying VED, laser power, scan speed, and linear energy density (LED), while keeping the rotation angle, stripe width, hatch distance, and layer thickness constant. From these, 17 samples exhibiting a relative density greater than 98% were selected for further analysis, ensuring minimal internal voids and porosity. This design of experiment facilitated a systematic study of the relationships between process parameters and resulting material properties.

Table 3.1: The process parameters used for the fabrication of the 45 samples

Parameter	Value
Layer Thickness (mm)	0.02
Hatch Distance (mm)	0.06
Stripe Width (mm)	5
Rotation Angle (degrees)	67°
Laser Power (W)	90 – 170
Scan Speed (mm/s)	600 – 1400

3.2 Composition of the powder

The powder used for PBF-L consist of primarily of Fe-6.5 wt% Si. This composition was selected for its desirable soft magnetic properties. Before processing, the powder was sieved and thoroughly mixed to ensure uniform particle distribution. No additional alloying elements were introduced, as the focus was on investigating the effect of energy density and build orientation on anisotropic behaviour and magnetic properties.

3.3 Printing of Samples

The samples were fabricated using an EOS M100 3D printer via the PBF-L process. Five cubic specimens with each cube dimension of $6 \times 6 \times 6$ cm^3 were produced as shown in Figure 3.1. The rotational angle of 67°, layer thickness of 0.02 mm, hatch distance of 0.06 mm, and stripe width of 5mm were maintained as constant process

parameters for all builds. In contrast, the laser power, scan speed, LED, and VED were systematically varied to investigate their effects.

Figure 3.1: Fabricated samples with each build contains 5 process parameter combinations.

3.4 Characterization techniques

3.4.1 Sample Preparation

The printed samples were sectioned using an IsoMet High Speed Pro precision cutter (Buehler) along the BD (front face or X-Z plane) and perpendicular to the BD (top face or X-Y plane) as shown in Figure 3.2 to investigate anisotropy along different axes.

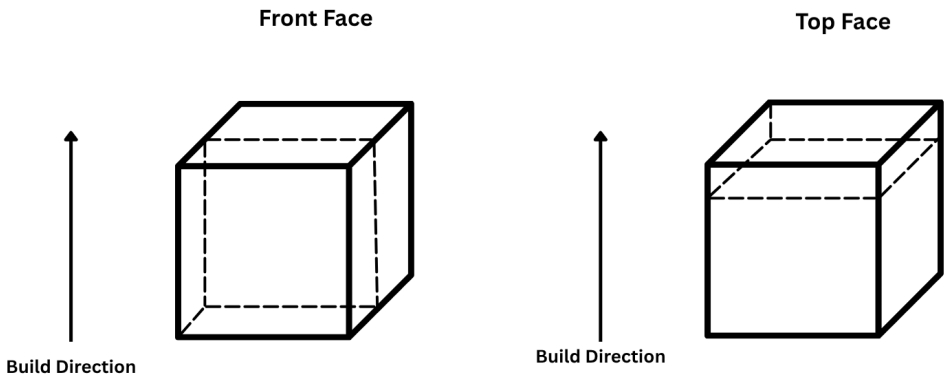

Figure 3.2: The Fe-6.5wt% Si cube samples cut along front face (X-Z Plane) and top face (X-Y Plane).

The samples were then mounted using a Struers CitoPress-20 hot mounting press with PolyFast resin. Subsequently, the mounted samples were polished on a Struers TegraPol-31 using progressively finer abrasives (9 μm, 3 μm, and 1 μm) to achieve the desired surface finish.

3.4.2 Optical Microscopy (OM)

OM was used to evaluate surface morphology, porosity, and relative density in the X-Z plane (front face) as shown in Figure 3.3. Images were captured at 10× and 20× magnifications and processed using ImageJ software.

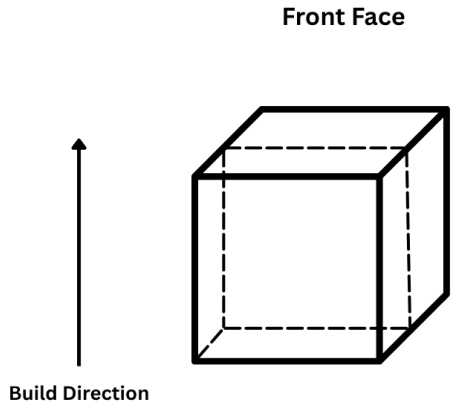

Figure 3.3: Schematic representation of Fe-6.5Wt% Si cubes sample cut along the BD (X-Z plane).

3.4.3 Vickers Hardness (HV)

Hardness measurements were carried out on a Durascan-70 G5 automated tester using a Vickers indenter with a load of HV0.3, and the resulting indentations were imaged at 20× magnification. The measurements were taken along two orientations: along the BD (X-Z plane) and perpendicular to the BD (X-Y plane), as illustrated in Figure 3.4. For each sample, approximately 30 indentations were performed, evenly distributed across the upper, middle, and lower positions termed as region 1, 2 and 3, respectively, of the sectioned samples (10 per region).

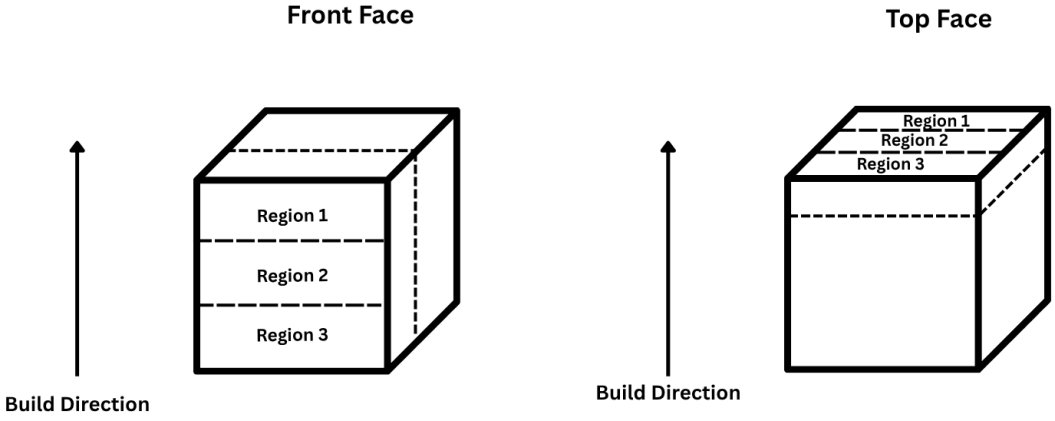

Figure 3.4: The Fe-6.5wt% Si cube samples cut along front face (X-Z Plane) and top face (X-Y Plane) for hardness measurement.

3.4.4 Vibrating Sample Magnetometer (VSM)

The magnetic properties of the sectioned samples were measured from the hysteresis loop (M-H curve), using the 8600 Series Vibrating Sample Magnetometer by LakeShore Cryotronics at room temperature. The magnetic properties of the prepared Fe–6.5 wt% Si samples sectioned along the X-Z plane were measured for samples with the magnetic field applied both parallel and perpendicular to the BD, as illustrated in Figure 3.5.

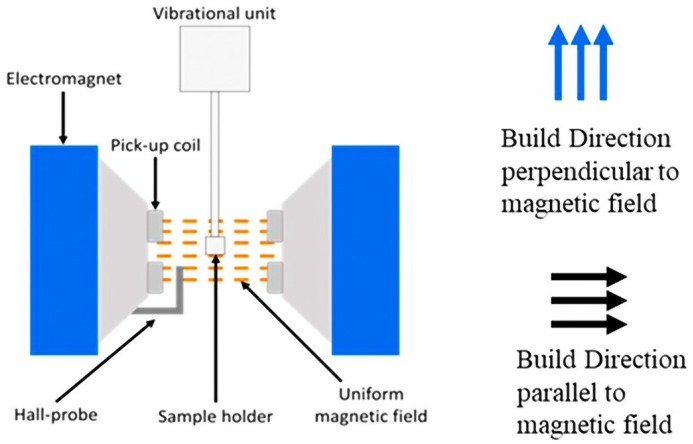

Figure 3.5: The working principle of VSM, with the BD of the sample aligned parallel and perpendicular to the field [7].

3.4.5 Electrical Resistivity (ρ)

The ρ of the samples was measured using the CMT-SR2000N four-point probe (Changmin Tech). Measurements were taken along two orientations: the BD (X-Z plane) and perpendicular to the BD (X-Y plane), as illustrated in Figure 3.4. For each sample, approximately 15 measurements were performed, evenly distributed across the upper, middle, and lower positions of the sectioned samples (5 per region).

3.4.6 XRD Analysis

Phase composition and crystallographic texture were characterized using XRD. The measurements were performed using a Bruker D8 Discover diffractometer with Cu Kα radiation ($\lambda = 1.54$ Å). Data were collected in the 2θ range of 20°–90° with a step size of 0.2 s in continuous coupled scan mode. The measurements were performed along the BD (X-Z plane) and perpendicular to the BD (X-Y plane) as shown in Figure 3.2.

4

Results and Discussion

4.1 Relative Density Analysis

Relative density was measured in the X–Z plane (along BD), as illustrated in Figure 3.3. For each sample, optical images were captured and analyzed using ImageJ software to evaluate the relative density of the fabricated samples. Figure 4.1 illustrates the relative density obtained at different VED values. Even a slight increase in the relative density percentage results in a significant improvement in surface morphology, with reduced defects. The lower laser power and a high scan speed can lead to the lack of fusion defects due to insufficient consolidation of the material [7]. The findings by [7] showed a similar relative density of 99.5% when laser power of 180 W, scan speed of 900 mm/s, hatch distance of 0.08 mm, layer thickness of 0.05 mm and laser beam diameter of 50 µm. The VED calculated based on their process parameter is 50 J/mm^3, which had the lowest porosity and cracking. This suggests the importance of the laser beam diameter in achieving higher relative density, which determines the energy density input on the sample surface.

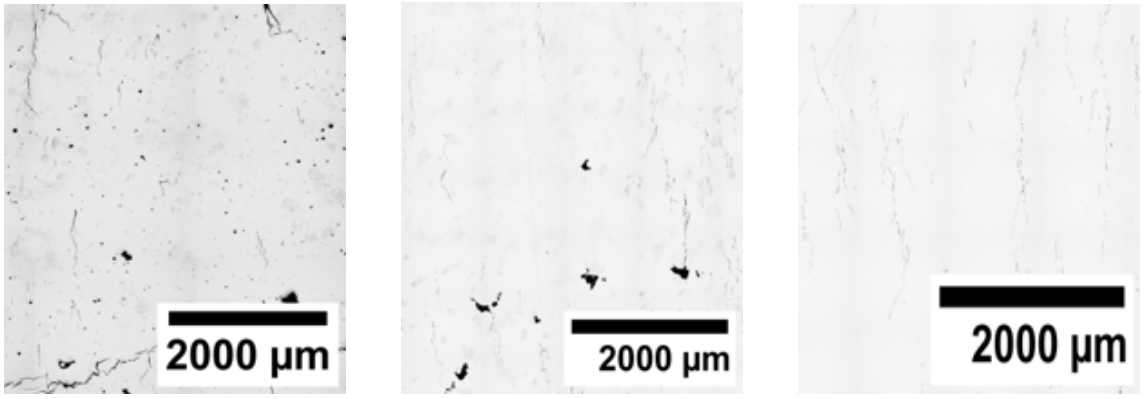

(a) Relative density of 98.14% at 125 J/mm^3.

(b) Relative density of 99.09% at 91.67 J/mm^3.

(c) Relative density of 99.44% at 111.11 J/mm^3.

Figure 4.1: Optical Microscope images of the sectioned samples in X-Z plane showing relative density obtained at different VEDs.

The following relative density trends were observed from Figure 4.2:

- The relative density ranged between 98.1% and 99.4% for the VED range between 90.28 to 222.22 J/mm^3.

- The maximum relative density of 99.4% was observed at the process parameter of laser power at 160 W, scan speed of 1200 mm/s and VED of 111.11 J/mm^3. The lowest relative density of 98.1% was obtained at a laser power of 90 W, scan speed of 600 mm/s and a VED of 125 J/mm^3.
- The optimal VED was in the range of 100–135 J/mm^3, with a relative density of $\geq$99% in almost all the samples. At a VED of 125 J/mm^3, samples exhibited varying relative densities despite having the same energy input. This implies that the laser power and scan speed plays a crucial role in achieving higher relative density.
- For the laser power in the range of 130–160 W, the samples printed showed a consistently high density. For the scan speed in the range of 1000–1200 mm/s, the samples printed showed minimal defects.

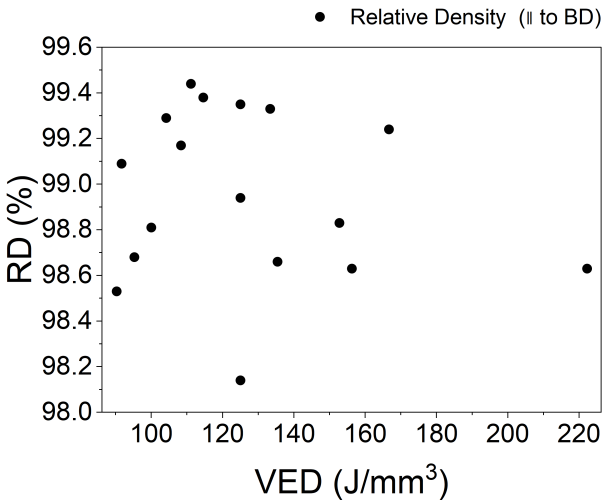

Figure 4.2: Relative Density vs. VED in X-Z plane.

Figure 4.2 shows the scatter plot of the relative density obtained for the corresponding VED used. We could observe a dense concentration of data points in the VED of 100 - 140 J/mm^3 above a relative density of 90%. Additionally, we observed the scattering of data points from the VED range of 90 to 222.22 J/mm^3. This is primarily due to the complex interaction between scan speed, laser power, hatch spacing, layer thickness, VED and the resulting melt pool stability [28]. However, it is crucial to optimise the VED utilised, as a combination of high laser power with slow scan speed can lead to keyhole porosity due to the melt pool vapourisation.

4.2 Magnetic Properties

The magnetic properties of the sectioned samples along the X-Z plane were investigated to evaluate the influence of anisotropy across different regions. Each sectioned sample was divided into two specimens, referred to as region 1 and region 2, relative to the BD as illustrated in Figure 4.3. Magnetic measurements were conducted in both parallel and perpendicular directions with respect to the applied field. The comparison between region 1 and region 2 provides insight into the effects of thermal gradients along the build height.

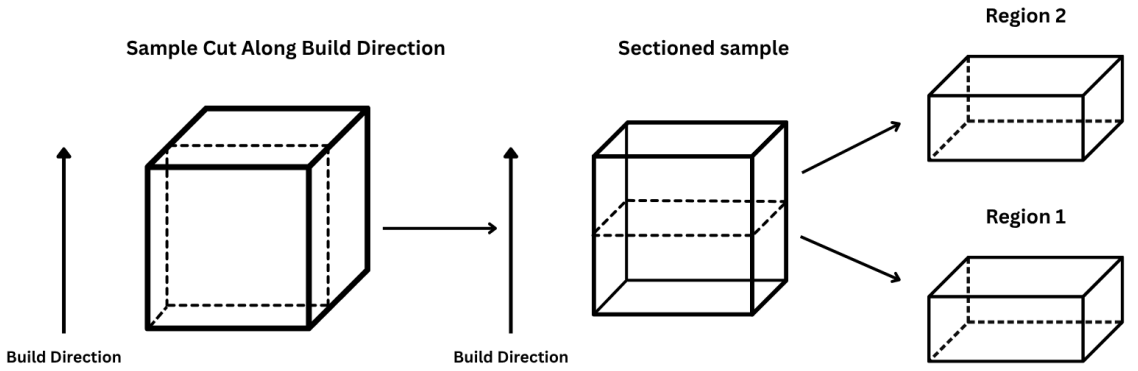

Figure 4.3: Schematic representation of region 1 and 2 after cutting operation.

The bottom layers experience greater heat accumulation and slower cooling, whereas the top layers solidify more rapidly. Evaluating these regions provides an understanding of the homogeneity throughout the produced samples. The comparison of magnetic properties between the top and bottom layers is essential for assessing the influence of residual stresses and microstructural variations along the build axis.

4.2.1 Saturation Magnetization (M_s) in Region 1 and 2

In region 1 of the sectioned sample, the following M_s trends were observed for the corresponding VEDs shown in Figure 4.4:

- The M_s was in the range of 172.4 emu/g to 202.4 emu/g with field parallel to BD and 165.7 emu/g to 202.4 emu/g with field perpendicular to BD.
- The M_s in region 1 showed the M_s was slightly higher with BD parallel to the field than perpendicular to the field. The VED in the range of 133.33 to 156.25 J/mm^3 showed the largest difference with a mean of 9.5 emu/g between parallel and perpendicular directions, indicating significant anisotropy in this VED range.
- The maximum M_s of 202.35 emu/g was obtained at VED of 95.24 J/mm^3, in both parallel and perpendicular to the field. The minimum M_s of 172.4 and 168.9 emu/g in parallel and perpendicular to the field was obtained at VED of 156.25 J/mm^3 and 152.78 J/mm^3, respectively.

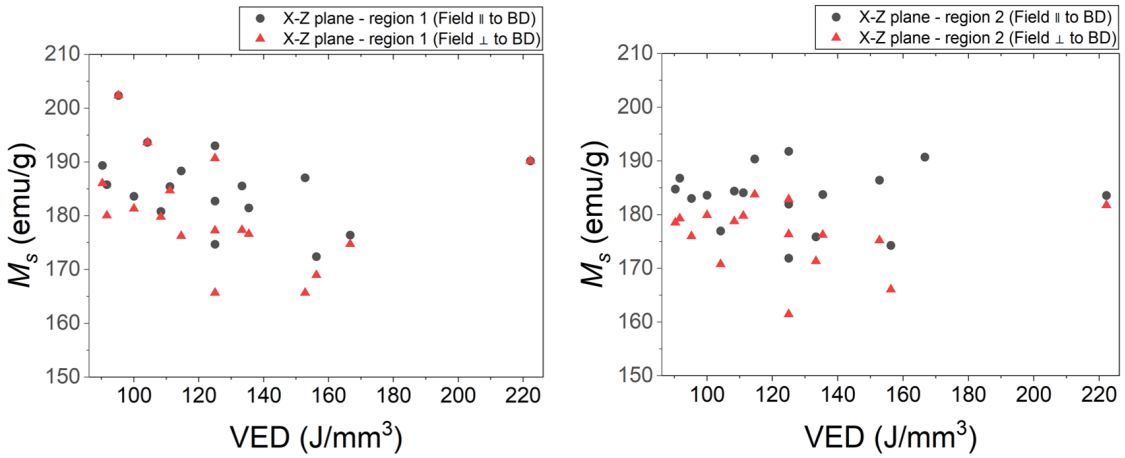

Figure 4.4: Comparison of M_s vs. VED in regions 1 and 2 of the sectioned samples.

In Region 2 of the sectioned sample, the following M_s trends were observed for the corresponding VEDs shown in Figure 4.4:

- The M_s was in the range of 171.9 emu/g to 191.8 emu/g with field parallel to BD and 161.5 emu/g to 183.7 emu/g with field perpendicular to BD.
- The M_s in Region 2 showed that M_s was generally slightly higher with BD parallel to the field than perpendicular to the field applied. The VED in the range of 133.33 to 156.25 J/mm^3 showed moderate anisotropy, with a mean between parallel and perpendicular directions ranging up to 8.7 emu/g, indicating directional dependence in this VED range.
- The maximum M_s of 191.8 emu/g was obtained at VED of 125 J/mm^3 in the parallel direction, while the maximum M_s of 183.7 emu/g was observed at VED of 114.58 J/mm^3 in the perpendicular direction. The minimum M_s of 171.9 emu/g (field parallel to BD) and 161.5 emu/g (field perpendicular to BD) was obtained at VED of 125 J/mm^3.

The M_s in both region 1 and region 2 shows directional dependence with respect to the VED. In region 1, M_s increases with VED in the range of 95–135 J/mm^3, reaching a maximum of 202.4 emu/g at 95.24 J/mm^3 and remains stable. The M_s achieves a higher value with 190.2 emu/g at a maximum VED of 222.22 J/mm^3. In contrast, region 2 exhibits much more stable M_s across the VED range of 90–152 J/mm^3 and achieves a maximum M_s of 191.79 emu/g at 125 J/mm^3 with lesser variation.

In regions 1 and 2, the magnetization is higher when the field is applied parallel to BD. The influence of VED is significant in region 1 than in region 2, due to the thermal accumulation as several layers are being deposited. The intermediate VED range favours increased M_s in region 1, while region 2 shows less effect. Thus, showing the complex interaction between VED conditions and the magnetic behaviour obtained across the build height of the sample.

A similar trend has been reported by [8], who used PBF-L to process Fe-3.8 wt% Si transformer steel. In their study, higher M_s was observed along the parallel direction (219 emu/g) compared to the perpendicular direction (205 emu/g). This behaviour is primarily attributed to the formation of a columnar grain structure aligned along the BD of the specimen, as shown in Figure 4.6. The slight reduction in M_s observed in the present study can be attributed to the addition of up to 6.5 wt% Silicon to iron. According to [11], the incorporation of 3 wt% Silicon can lead to a reduction in M_s by approximately 10%.

4.2.2 Coercivity (H_c) in Region 1 and 2

In region 1 of the sectioned sample, the following H_c trends were observed for the corresponding VEDs shown in Figure 4.5:

- The overall H_c values ranged from 1.4 to 3.1 Oe with the field parallel to the BD, and from 1.7 to 3.1 Oe with the field perpendicular to BD. The H_c in region 1 was lower with BD parallel to the field than perpendicular to the field in most of the VED conditions.
- In region 1 with field parallel to the BD, the lowest H_c of 1.4 Oe was obtained at 133.33 J/mm^3. With the field perpendicular to the BD, the lowest H_c of 1.7 Oe was obtained at 125 J/mm^3.
- In region 1 with field parallel to the BD, the highest H_c of 3.1 Oe was obtained at 95.24 J/mm^3, whereas with the field perpendicular to the BD, the highest H_c of 3.1 Oe was obtained at 152.78 J/mm^3.

In region 2 of the sectioned sample, the following H_c trends were observed for the corresponding VEDs shown in Figure 4.5:

- The overall H_c values ranged from 1.3 to 2.6 Oe with the field parallel to the BD, and from 1.6 to 3.1 Oe with the field perpendicular to the BD. Similar to region 1, the H_c in region 2 was generally lower when the field was applied parallel to the BD.
- In region 2 with the field parallel to the BD, the lowest H_c of 1.3 Oe was obtained

at a VED of 111.11 J/mm³. In contrast, with the field applied perpendicular to the BD, the lowest H_c of 1.6 Oe was obtained at a VED of 152.78 J/mm³.

- In region 2 with the field parallel to the BD, the highest H_c of 2.6 Oe was obtained at a VED of 95.24 J/mm³. Meanwhile, for the field applied perpendicular to the BD, the highest H_c of 3.1 Oe was recorded at a VED of 133.33 J/mm³.

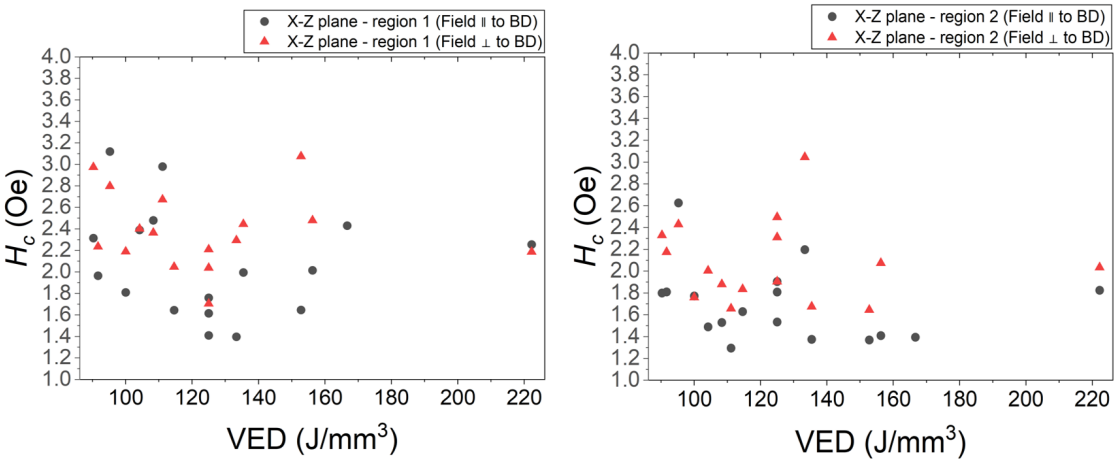

Figure 4.5: Comparison of H_c vs. VED in regions 1 and 2 of the sectioned samples.

The H_c in both region 1 and region 2 shows a strong correlation with the VED utilized. In region 1 with field parallel to BD, the H_c decreases drastically from the VED range of 90.28 to 133.3 J/mm³ and increases with further increase in VED, with the lowest H_c of 1.4 Oe obtained at 133.3 J/mm³. Thus, forming a U-shaped trend and showing a strong correlation with the VED. When the field is perpendicular to BD, the H_c decreases from 90.28 to 125 J/mm³ and stabilizes with further increase in VED.

In region 2 with field parallel to BD, the H_c decreases steadily from the VED range of 90.28 to 156.25 J/mm³. When the field is perpendicular to BD, there is a similar decrease in VED, but the H_c peaks in the VED of 133.33 J/mm³.

The study by [27] further emphasized that defects and grain size distribution play a critical role in determining the magnetic properties. A higher number of grain boundaries, cracks and porosity acts as pinning sites for domain walls, thereby obstructing their motion during magnetization and demagnetization and consequently increasing H_c with BD perpendicular to the field than parallel to the field.

Comparison of region 1 and region 2 in the sectioned samples revealed a clear variation in magnetic properties, with region 2 exhibiting better soft-magnetic behaviour. In PBF-L, the thermal profile of a printed part strongly depends on build height, since each layer undergoes multiple thermal cycles during the layer-by-layer consolidation of Fe–6.5 wt% Si powder. In region 1, the material experiences extensive reheating due to repeated thermal cycling. Each newly deposited layer partially remelts the underlying solidified layers, which reduces the cooling rate (R) and lowers the thermal gradient (G). The combined effect decreases the G/R ratio, promoting the growth of coarser columnar grains with weaker crystallographic texture [6, 14]. Moreover, successive heat input generates residual stresses that further degrade magnetic performance [27].

In contrast, region 2 experiences less reheating and lower thermal accumulation, since fewer layers are deposited above it. This condition results in faster post-solidification cooling and reduced residual stress. A higher cooling rate, combined with a steeper temperature gradient, increases the G/R ratio and favours the formation of finer grains with a pronounced $\langle 100 \rangle$ crystallographic orientation [6]. Thus, enhancing domain-wall movement and lowering H_c [14].

The Fe–6.5 wt% Si samples exhibited distinct direction-dependent magnetic behaviour, with M_s and H_c consistently showing superior performance when the field applied was parallel to the BD compared to the perpendicular orientation. According to [8], the formation of columnar grain morphology, reduced grain-boundary density, and a preferred $\langle 100 \rangle$ texture along the BD facilitate domain wall motion and promote complete alignment of magnetic dipoles. In contrast, the presence of $\langle 101 \rangle$ and $\langle 111 \rangle$ crystallographic orientations makes magnetization more difficult and leads to higher H_c. Hence, the M_s is significantly higher and H_c lower in the parallel direction compared to the perpendicular direction of the applied field.

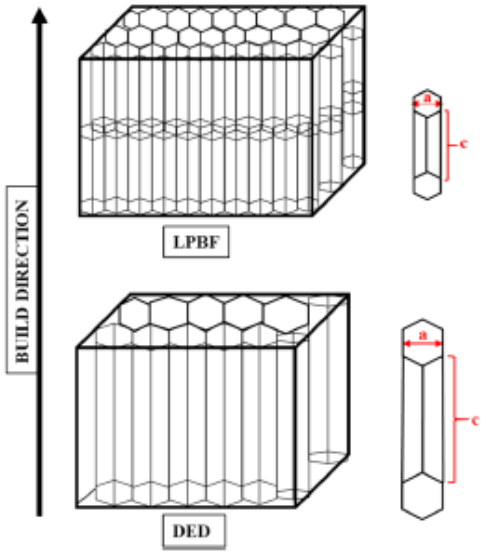

Figure 4.6: The columnar morphology produced along BD in PBF-L and DED AM process [8].

4.3 Hardness

4.3.1 Hardness in Whole sample of X-Z and X-Y Plane

The overall average of hardness for the whole region in the X-Z plane is 388.6 ± 9.1 HV, and in the X-Y plane is 387.2 ± 8.9 HV. The average difference between the two planes is 1.4 HV, and the relative difference of 0.36%. In most VED conditions, the hardness is slightly higher in the X-Z plane as shown in Figure 4.7. In the VED range of 125 - 160 J/mm^3, the hardness between X-Z and X-Y is higher comparatively, with a difference of approximately 5-10 HV. Thus, the effect of VED is much higher in the mid-range, comparatively, due to the higher thermal gradient and causes increased grain boundary density along the BD. From the VED parameters used, the material doesn't produce a weaker hardness in a particular direction.

Table 4.1: HV obtained in X–Z and X–Y planes at different VEDs.

Plane	Hardness Range (HV)	Max. Hardness (HV)	VED (Max. Hardness) (J/mm^3)	Min. Hardness (HV)	VED (Min. Hardness) (J/mm^3)
X–Z	381.9 – 396.1	396.1	125.00	381.9	108.33
X–Y	379.4 – 394.7	394.7	100.00	379.4	91.67

The hardness values measured in the X–Z and X–Y planes exhibited a similar range as shown in Table 4.1. This difference is attributed to the greater influence of thermal gradients along the build height (X–Z plane), which results in increased residual stresses, grain refinement, and restricted dislocation movement. In contrast, the X–Y plane represents measurements taken across the same build layer, where thermal gradients are more uniform and exert less influence, leading to more stable hardness values across the plane.

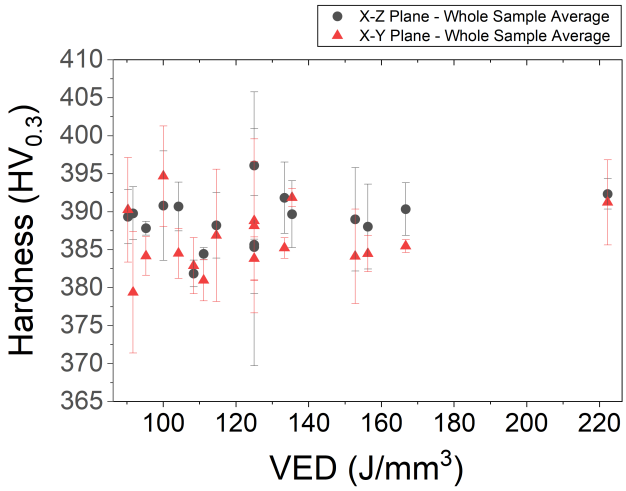

Figure 4.7: Comparison of HV vs.VED for the whole sample in X-Z and X-Y plane.

This behaviour across different build orientations is consistent with the observations of [29], who produced Fe–3 wt% Si samples using optimized process parameters. The study by [30] reported a hardness value comparable to the present findings of 389 HV, with 371.5 HV measured for Fe–5.5wt% Si. The observed increase in hardness with silicon addition is attributed to the solid solution strengthening of the BCC iron lattice by silicon atoms [17]. The brittle behaviour observed in the samples is not a result of process parameters in PBF-L, but rather due to the material's characteristics.

4.3.2 Hardness in regions 1, 2 and 3 of X-Z and X-Y Plane

The optimal VED range was identified as 100–135.42 J/mm³as shown in Table 4.2, within which hardness values across all three regions remained generally stable. However, Region 2 showed noticeable deviations at 114.58 J/mm³ and 125.00 J/mm³ in both planes, with the latter producing a pronounced peak hardness of 406.6 HV in X-Z plane.

Table 4.2: Maximum and minimum HV measured in X–Z and X–Y planes for regions 1, 2 and 3 at varying VEDs.

Region	Plane	Max. Hardness (HV)	VED (Max. Hardness) (J/mm³)	Min. Hardness (HV)	VED (Min. Hardness) (J/mm³)
1	X–Z	397.9	100.00	378.9	125.00
1	X–Y	393.5	100.00	370.4	91.67
2	X–Z	406.6	125.00	383.3	114.58
2	X–Y	401.8	100.00	375.4	125.00
3	X–Z	394.4	135.42	370.1	125.00
3	X–Y	397.8	125.00	380.1	111.11

The variation in hardness observed across Regions 1, 2, and 3 of the X-Z and X-Y plane, as shown in Figure 4.8 at the different VEDs, is primarily attributed to the influence of residual stress formation, microstructural growth, and the development of ordered phases, which collectively determine the hardness in different regions [17, 30]. In the X-Y plane at a lower VED of 91.67 J/mm³, a significant decline in hardness is observed, with 370.4 HV reported in Region 1. This reduction could be attributed to the presence of defects such as cracks and irregular pores resulting from insufficient energy input to fully melt the powder. Thus, reducing the solid-solution strengthening mechanisms of the Fe–6.5 wt% Si powder [29].

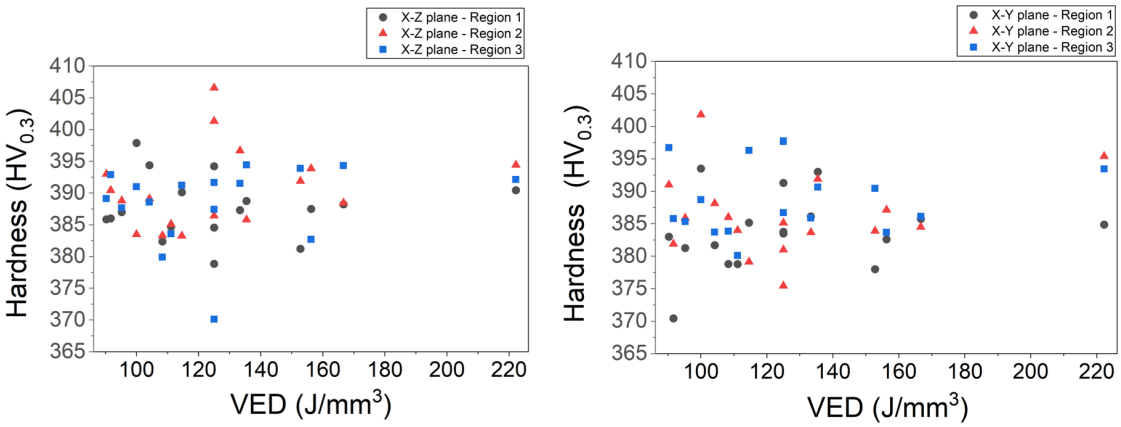

Figure 4.8: Comparison of HV vs.VED for the regions 1, 2 and 3 in X-Z and X-Y plane.

According to Figure 4.8, in the X-Z plane, for VED >135 J/mm³, region 3 has higher hardness and has an average hardness increase of 8.5 HV. The hardness in the VED range of 115-135 J/mm³ exhibits significant variation, with an average hardness increase of 16.1 HV and region 2 consistently exhibits the highest hardness. For VED <115 J/mm³, there is no consistent region having higher hardness and has an average hardness range of 5.8 HV. In X-Z plane at VED of 95.24 J/mm³, the mean hardness of 387.83 HV, SD of 0.7 HV and the range of 1.8 HV was observed.

In the X-Y plane, for VED >135 J/mm³, there is no consistent region having higher hardness and has an average hardness increase of 6.3 HV. Thus, ensuring reliable homogeneity across the regions 1, 2 and 3. The hardness in the VED range of 115-135 J/mm³ exhibits high variability, with an average value of 12.4 HV. Region 3 consistently exhibits higher hardness, with varying magnitudes. In VED <115 J/mm³, region 2 consistently shows the highest hardness. In X-Y plane at VED of 166.67 J/mm³, the mean hardness of 385.5 HV, SD of 0.9 HV and range of 1.6 HV was observed. Thus, optimizing the VED parameter reduces regional variation and can be used to produce highly homogeneous components.

The influence of VED in the X-Z and X-Y planes demonstrates that VED plays a critical role in controlling the mechanical properties. In the X-Z plane, VED >135 J/mm³ and in the X-Y plane, VED <115 J/mm³ yield better results due to the improved homogeneity across the planes.

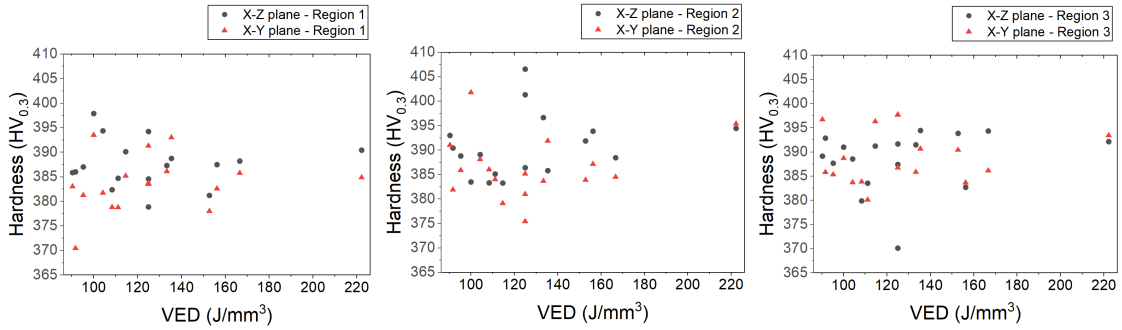

Figure 4.9: Region-wise comparison of HV vs.VED for the regions 1, 2 and 3 in X-Z and X-Y plane.

From Figure 4.9, region 2 shows a significant difference in hardness between the X-Z and X-Y planes, and the hardness is more pronounced in X-Z plane. In region 1 and region 3, the difference in hardness between X-Z and X-Y planes is about 2.3 HV and 1.3 HV, respectively. There is no specific region showing higher hardness.

The one-way analysis of variance (ANOVA) conducted on the 17 samples showed that build orientation had no statistically significant influence on the microhardness, as shown in Table 4.3. The measurement showed that parallel to the BD $F(2, 150) = 1.45$, $p = 0.24$ and perpendicular to the BD $F(2, 150) = 1.82$, $p = 0.17$.

Table 4.3: One-Way ANOVA results for HV in X-Z and X-Y plane.

Plane	Variation Source	Sum of Squares	Mean Square	F-value	p-value
X–Z	Between Regions (R1, R2 and R3)	216.45	108.22	1.45	0.24
X–Z	Within Regions (Error)	11182.17	74.55	–	–
X–Z	Total Variation	11398.62	–	–	–
X–Y	Between Regions (R1, R2 and R3)	324.68	162.34	1.82	0.17
X–Y	Within Regions (Error)	11204.21	89.36	–	–
X–Y	Total Variation	11528.89	–	–	–

4.4 Resistivity

4.4.1 Resistivity in Whole sample of X-Z and X-Y Plane

The overall average of ρ for the whole region in the X-Z plane is 105.8 ± 23.9 μΩ · cm and in the X-Y plane is 100.6 ± 25.9 μΩ · cm. The average difference between both planes is 5.2 μΩ · cm.

Table 4.4: Maximum and minimum ρ values in X–Z and X–Y planes at different VEDs.

Plane	ρ Range (μΩ · cm)	Max. ρ (μΩ · cm)	VED (Max. Hardness) (J/mm³)	Min. ρ (μΩ · cm)	VED (Min. Hardness) (J/mm³)
X–Z	71.9 – 155.4	155.4	111.11	71.9	114.58
X–Y	74.7 – 143.7	143.7	135.42	74.7	125.00

In the X-Z plane, the ρ reached a maximum of 155.4 μΩ · cm at VED of 111.11 J/mm³, as shown in Table 4.4. From Figure 4.10, the VED showed no consistent trend and fluctuated across the VED ranges. In the X-Y plane, the ρ changes abruptly between samples. The ρ varied significantly in three samples produced using the same VED of 125 J/mm³, with each having 74.7 μΩ.cm, 85 μΩ.cm and 115.6 μΩ.cm. Thus, the parameters such as laser power and scan speed used to achieve the same VED also plays a critical role in the formation of microstructure and the resulting ρ.

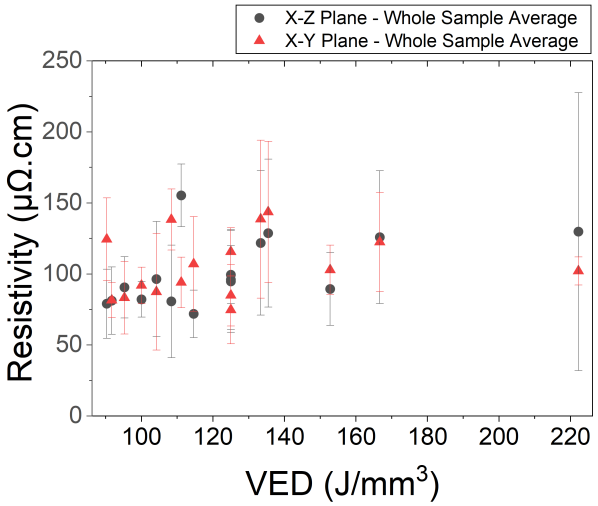

Figure 4.10: Comparison of HV vs.VED for the whole sample in the X-Z and X-Y plane.

The VED shows no statistically significant correlation with ρ in both X-Z and X-Y planes. The X-Z plane showed higher variation with an SD of 25.9 μΩ · cm, and X-Y showed an SD of 20.5 μΩ · cm. The X-Z plane showed 26% greater variability than X-Y due to higher sensitivity to microstructural variations along the build height.

The pronounced thermal gradient along the BD induces residual stresses throughout the build height, which in turn promotes the formation of cracks and finer grains [15].

Table 4.5: The Pearson Correlation Coefficients (r) for VED vs. ρ

Plane	Pearson Correlation (r)	Interpretation	Conclusion
X–Y	-0.19	Negligible Negative Correlation	No meaningful relationship.
X–Z	+0.09	Negligible or No Correlation	No linear relationship.

The Pearson correlation analysis, as shown in Table 4.5, provides no statistically significant linear relationship with ρ in both the X-Z and X-Y planes. The Pearson correlation (r) of -0.19 in the X-Y plane indicates a minimal tendency for ρ to decrease with an increase in VED. The r of +0.09 in the X-Z plane indicates a minimal tendency for ρ to increase with a decrease in VED. The calculated r values are within the negligible range and are too weak to be significant.

Thus, VED alone is not a sufficient predictor of ρ across different orientations. A more reliable understanding requires considering the combined effects of laser power, scan speed, and the resulting melt-pool morphology and grain boundary characteristics. Mapping these interactions provides a more complete representation of ρ trends and enables more effective mitigation of anisotropy for improved performance.

4.4.2 Resistivity in regions 1, 2 and 3 of X-Z and X-Y Plane

The overall average ρ in the X-Z plane for the regions 1, 2 and 3 is 131.4 $\mu\Omega \cdot cm$, 116.1 $\mu\Omega \cdot cm$ and 111.6 $\mu\Omega \cdot cm$, respectively, and in the X-Y plane for the regions 1, 2 and 3 is 148 $\mu\Omega \cdot cm$, 94.1 $\mu\Omega \cdot cm$ and 107.3 $\mu\Omega \cdot cm$, respectively. Table 4.6 shows the maximum and minimum ρ obtained at different VEDs.

Table 4.6: ρ Range and Corresponding VED Values by Region and Plane

Region	Plane	ρ Range ($\mu\Omega \cdot cm$)	Max. ρ ($\mu\Omega \cdot cm$)	VED (Max. Hardness) (J/mm^3)	Min. ρ ($\mu\Omega \cdot cm$)	VED (Min. Hardness) (J/mm^3)
1	X–Z	80.4 – 182.3	182.3	222.22	80.4	100.00
1	X–Y	86.7 – 209.3	209.3	133.33	86.7	91.67
2	X–Z	58.9 – 173.2	173.2	133.33	58.9	108.33
2	X–Y	59.5 – 128.7	128.7	166.67	59.5	104.17
3	X–Z	58.7 – 164.5	164.5	111.11	58.7	222.22
3	X–Y	64.1 – 150.4	150.4	135.42	64.1	95.24

The variation in ρ observed across regions 1, 2, and 3 of the X-Z and X-Y plane at the different VED is shown in Figure 4.11. In the X-Z plane, region 1 shows an inconsistent trend with VED with high variation. At a higher VED of 222.22

J/mm³, the maximum ρ of 182.34 µΩ.cm was obtained with a SD of 106.41 µΩ.cm in comparison with other regions 2 and 3. Region 2 showed the highest variation with no consistent trend to VED. Thus, making it sensitive to the process parameters with an unstable melt pool due to the residual heat from previous layers. Region 3 shows the lowest and stable ρ, suggesting consistent thermal conditions leading to fewer defects and less scattering of electrons.

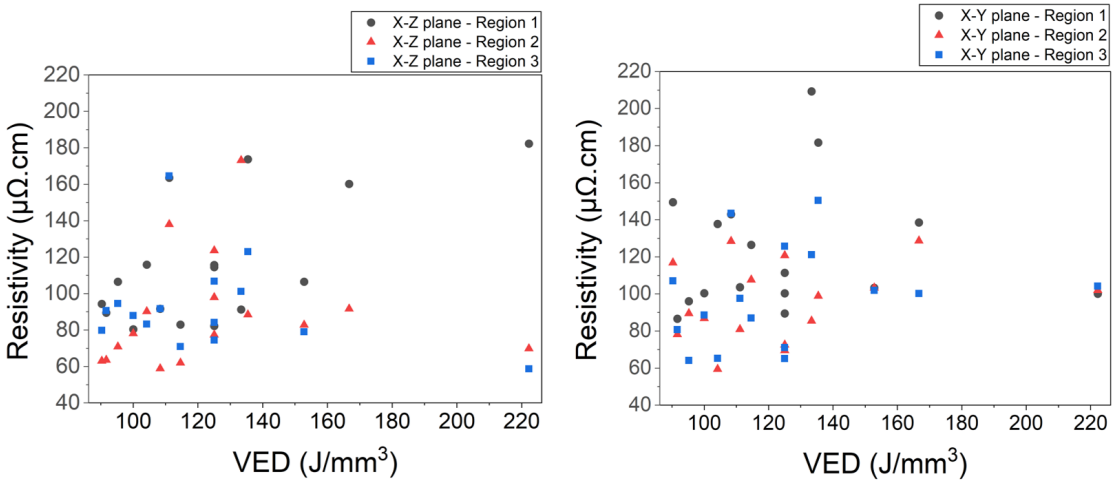

Figure 4.11: Comparison of ρ vs.VED for the regions 1, 2 and 3 in X-Z and X-Y plane.

In the X-Y plane, region 1 shows a positive correlation with VED with an r of +0.41. The ρ increases with an increase in VED and with moderate SD. Region 2 shows much more stable ρ in the cluster of 70-130 µΩ.cm without any outliers. Region 3 doesn't show a strong correlation with VED, but at higher VED, the ρ decreases, suggesting a lesser occurrence of defects such as vaporization.

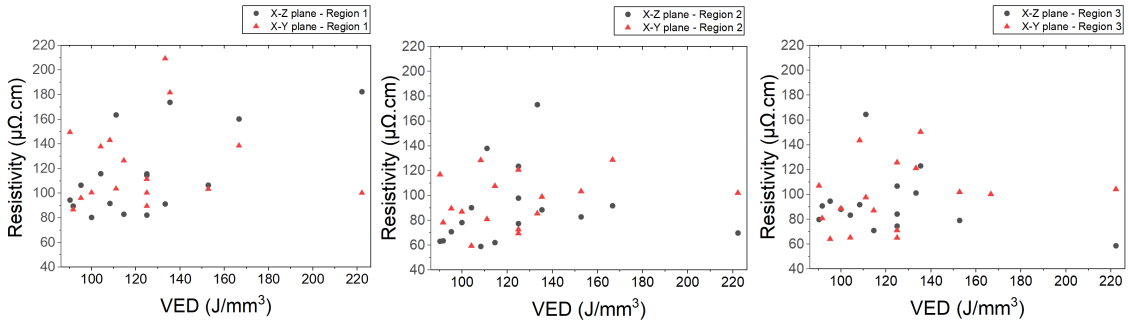

Figure 4.12: Region-wise comparison of ρ vs.VED for the regions 1, 2 and 3 separately in X-Z and X-Y plane.

The comparison of ρ in X-Z and X-Y planes shows that the local variations in thermal gradients across regions cause variations in grain structure, defect density, and melt pool morphology. Thus, leading to significant variation in ρ along the planes. In the X-Z plane, the spatial inhomogeneity of in-plane properties with high

variability shows that ρ will be location-dependent. In the X-Y plane ρ shows better stability and homogeneity.

From Figure 4.12, region 2 in the X-Z plane showed the largest range ρ from 58.9 to 173.2 $\mu\Omega \cdot$ cm, with no consistent trend with VED. Region 1 of the X-Z plane, the ρ showed strong correlation with VED and attained the highest ρ 181.7 $\mu\Omega \cdot$ cm. Region 3 consistently showed the minimum and most stable ρ. There is no specific region in either the X-Z or X-Y planes that provides enhanced ρ.

Table 4.7: Pearson Correlation Coefficients (r): VED vs. ρ by Region

Plane	Region	Pearson Correlation (r)	Interpretation	Conclusion
X-Z	Region 1	+0.25	Weak Positive	weak relationship.
X-Z	Region 2	-0.11	Negligible	No meaningful linear relationship.
X-Z	Region 3	-0.28	Weak Negative	weak relationship.
X-Y	Region 1	+0.41	Moderate Positive	Noticeable positive trend.
X-Y	Region 2	-0.19	Negligible / Very Weak	No linear relationship.
X-Y	Region 3	-0.17	Negligible / Very Weak	No linear relationship.

Table 4.7 presents the Pearson correlation coefficients in regions 1, 2, and 3 for the X-Z and X-Y planes. The r values obtained show that ρ is anisotropic and spatially heterogeneous in both planes. The VED shows a consistent trend in specific locations, such as region 1, in both planes.

4.5 Crystalline Structure

The XRD analysis was performed to identify the phases present in Fe–6.5 wt.% Si specimens taken from both the X-Z plane and X-Y plane of the cube, as shown in Figure 3.2. The samples representing three distinct VED levels, low (91.67 J mm^{-3}), medium (125 J mm^{-3}), and high (152.78 J mm^{-3}) were examined to evaluate possible phase variations across the VED range.
The XRD patterns from the figures 4.13, 4.14 and 4.15 revealed a single-phase BCC structure of α-Fe(Si), with characteristic diffraction peaks at the (110), (200), and (211) planes with no evidence of secondary or ordered phases such as B2 (ordered FeSi) or DO_3 (ordered Fe_3Si). This finding confirms the formation of a stable solid solution typical of Fe–6.5 wt.% Si in all the examined samples, sectioned both parallel and perpendicular to the BD.

The study by [7] utilised PBF-L to fabricate Fe–6.5 wt% Si transformer cores, where the XRD analysis shows identical diffraction peaks at (110), (200), and (211) planes corresponding to the BCC α-Fe(Si) phase and confirms a single-phase α-Fe(Si) with no presence of secondary or ordered phases such as B2 or DO_3. Additionally, their

study confirms the thermal stability of this phase even after post-processing activities, such as annealing at 1150 °C.

In contrast, [16] argued that unfavourable process conditions, such as thermal gradients, inhomogeneous cooling and elemental segregation during solidification, can lead to the formation of ordered phases, including B2 (ordered FeSi), DO_3 (ordered Fe_3Si) and Fe_3Si precipitates. This indicates that phase stability in Fe–6.5 wt% Si is highly sensitive to PBF-L process parameters. According to [31], the presence of a single-phase BCC structure is necessary to achieve desired magnetic behaviour such as high μ, low H_c, and reduced hysteresis losses. It is due to the facilitation of domain wall motion as a result of the reduction in pinning sites by BBC iron's open atomic arrangement. Also, the BCC lattice along the $\langle 100 \rangle$ directions allows easier realignment of magnetic domains under the magnetic field.

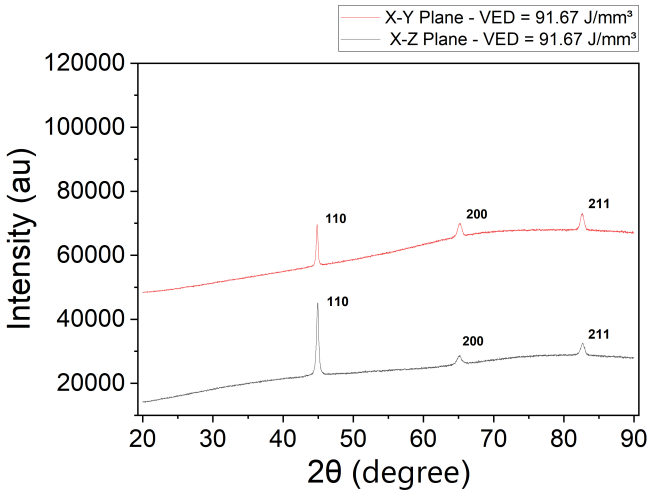

Figure 4.13: XRD pattern for the sample with VED of 91.67 J/mm³ in X-Z and X-Y plane.

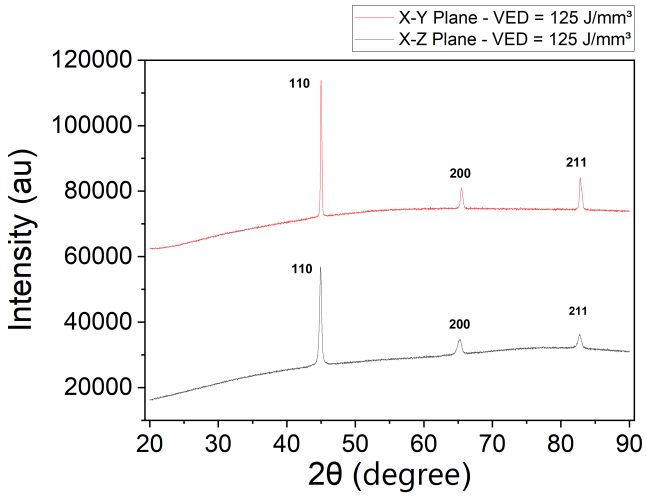

Figure 4.14: XRD pattern for the sample with VED of 125 J/mm^3 in X-Z and X-Y plane.

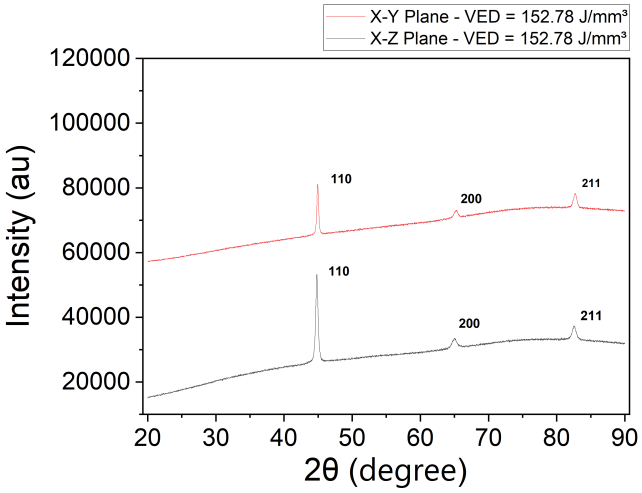

Figure 4.15: XRD pattern for the sample with VED of 152.78 J/mm^3 in X-Z and X-Y plane.

5

Conclusion

This study systematically investigated the effects of VED and the corresponding anisotropic behaviour of multi-property Fe–6.5 wt% Si alloys. The work focused on identifying correlations between processing parameters, microstructural evolution, and the resulting magnetic, mechanical, and electrical properties. Improving these properties in Fe–6.5 wt% Si alloy is essential to achieve high performance in demanding applications. The results demonstrate that VED plays a critical role in controlling solidification rate, formation of microstructural texture and the melt pool size. Magnetic characterization showed that the M_s and H_c showed dependence on VED and build orientation. In region 1, M_s reached a maximum of 202 emu/g at a VED of 95.24 J/mm^3, and H_c achieved a minimum value of 1.4 Oe at a VED of 133.33 J/mm^3, forming a U-shaped trend with VED variation. In Region 2, M_s reached a maximum of 191.79 emu/g at VED of 125 J/mm^3 and H_c with the lowest of 1.29 Oe at 111.11 J/mm^3. The results show that thermal gradient along BD in PBF-L causes significant variation in M_s and H_c. Hardness measurements exhibited a similar trend with varying VED, with the whole sample average hardness showed a maximum of 396 HV in the X-Z plane and 394 HV in the X-Y plane. The intermediate VED range of 100–125 J/mm^3 produced the highest hardness in both planes. The region 2 in both the planes showed the highest hardness compared to region 1 and region 3 in X-Z and X-Y planes.

ρ for whole sample in X–Z and X–Y planes showed a high variation with no strong correlation with VED. In the X–Z plane, ρ achieved a maximum of 155.4 $\mu\Omega \cdot$ cm at a VED of 111.11 J/mm^3 and in X-Y plane 143.7 $\mu\Omega \cdot$ cm at 135.42 J/mm^3. Resistivity shows a strong region-dependent variation in both planes. In the X-Z plane, region 1 exhibits the maximum $\wp$ of 182.34 $\mu\Omega \cdot$ cm and in X-Y plane, $\wp$ in region 1 shows a moderate increase with VED. The observed variation in ρ is highly sensitive to grain size and defects as a result of thermal accumulation in various regions of the sample. These findings demonstrate the effectiveness of using PBF-L to fabricate Fe–6.5 wt% Si alloys for next-generation electric motors, transformers, and high-frequency electromagnetic devices. They also provide valuable insights into AM strategies and further optimization for industrial applications.

5.1 Future Work

- Further studies should focus on the combined effects of power, scan speed, and VED to understand their collective influence on the microstructure and properties of the fabricated component.
- Establishing a correlation between laser fluence (energy per unit area) and VED (energy per unit volume) could offer deeper insights into the interactions affecting both surface and bulk material behaviour.
- Investigating post-processing techniques, such as annealing and hot isostatic pressing (HIP), is essential for improving component performance by minimizing anisotropy.
- Advanced characterization methods, such as Electron Backscatter Diffraction (EBSD), could be employed to gain a deeper understanding of the relationship between microstructure and material properties.
- The incorporation of alloy modifications and machine learning could be used to evaluate which process parameters yield the desired material properties across different axes.

Bibliography

[1] N. Giannotta, G. Sala, C. Bianchini, and A. Torreggiani, "A review of additive manufacturing of soft magnetic materials in electrical machines," *Machines*, vol. 11, no. 7, p. 702, 2023.

[2] W. Storr, "Magnetic hysteresis," 2024. Accessed: 2025-10-17.

[3] S. Sun, M. Brandt, and M. Easton, "Powder bed fusion processes: An overview," *Laser Additive Manufacturing*, vol. 2, pp. 55–77, 2017.

[4] MIT Department of Materials Science and Engineering, "Lecture 26: Magnetic domains," 2013. MIT OpenCourseWare, 3.024 Electronic, Optical and Magnetic Properties of Materials, Spring 2013.

[5] Krishnan and K. M., *Magnetic Anisotropy*. Oxford University Press, 2016.

[6] B. D. Cullity and C. D. Graham, *Introduction to magnetic materials*. John Wiley Sons, 2011.

[7] A. Z. Macknojia, J. V. Tran, M. P. Mckinstry, J. Galindo, Y. Jin, S. Dowden, S. M. Patil, M. V. Pantawane, K. M. Krishna, and R. Banerjee, "Additive manufacturing of fe-6.5 wt.% si transformer steel toroidal cores: Process optimization, design aspects, and performance," *Materials Design*, vol. 241, p. 112883, 2024.

[8] S. M. Varahabhatla, M. S. K. K. Y. Nartu, S. A. Mantri, V. Chaudhary, K. V. M. Krishna, S. S. Joshi, R. V. Ramanujan, N. B. Dahotre, and R. Banerjee, "Influence of energy density on the microstructure, growth orientation, and anisotropy of magnetic properties in additively manufactured fe-3.8wt%si transformer steels," *Materialia*, vol. 30, p. 101854, 2023.

[9] U. Goals, "Goal 13: Take urgent action to combat climate change and its impacts," 2019.

[10] G. Ouyang, X. Chen, Y. Liang, C. Macziewski, and J. Cui, "Review of fe-6.5 wt%si high silicon steel—a promising soft magnetic material for sub-khz application," *Journal of Magnetism and Magnetic Materials*, vol. 481, p. 234–250, 2019.

[11] Krishnan and K. M., *Hard and Soft Magnets*. Oxford University Press, 2016.

[12] K. Fujisaki, *Magnetic Material for Motor Drive Systems*. Springer, 2019.

[13] B. R. Rodriguez-Vargas, G. Stornelli, P. Folgarait, M. R. Ridolfi, A. F. Miranda Pérez, and A. Di Schino, "Recent advances in additive manufacturing of soft magnetic materials: A review," *Materials*, vol. 16, no. 16, p. 5610, 2023.

[14] Krishnan and K. M., *Introduction to Magnetism and Magnetic Materials*. Oxford University Press, 2016.

[15] W. H. Teh, L. P. Tan, S. Chen, F. Wei, J. J. Lee, S. P. Padhy, V. Chaudhary, C. C. Tan, and R. V. Ramanujan, "Breaking conventional limits of silicon

content in fe-xsi magnetic alloys through additive manufacturing," *Journal of Alloys and Compounds*, vol. 983, p. 173829, 2024.

[16] A. V. Agapovichev, A. I. Khaimovich, Y. A. Erisov, and M. V. Ryazanov, "Investigation of soft magnetic material fe-6.5 si fracture obtained by additive manufacturing," *Materials*, vol. 15, no. 24, p. 8915, 2022.

[17] A. Andreiev, K.-P. Hoyer, F. Hengsbach, M. Haase, L. Tasche, K. Duschik, and M. Schaper, "Powder bed fusion of soft-magnetic iron-based alloys with high silicon content," *Journal of Materials Processing Technology*, vol. 317, p. 117991, 2023.

[18] D. Dev Singh, T. Mahender, and A. Raji Reddy, "Powder bed fusion process: A brief review," *Materials Today: Proceedings*, vol. 46, p. 350–355, 2021.

[19] V. Chaudhary, S. A. Mantri, R. V. Ramanujan, and R. Banerjee, "Additive manufacturing of magnetic materials," *Progress in Materials Science*, vol. 114, p. 100688, 2020.

[20] T. DebRoy, H. L. Wei, J. S. Zuback, T. Mukherjee, J. W. Elmer, J. O. Milewski, A. M. Beese, A. Wilson-Heid, A. De, and W. Zhang, "Additive manufacturing of metallic components – process, structure and properties," *Progress in Materials Science*, vol. 92, p. 112–224, 2018.

[21] L. Tonelli, A. Fortunato, and L. Ceschini, "Cocr alloy processed by selective laser melting (slm): Effect of laser energy density on microstructure, surface morphology, and hardness," *Journal of Manufacturing Processes*, vol. 52, p. 106–119, 2020.

[22] S. Gorsse, C. Hutchinson, M. Gouné, and R. Banerjee, "Additive manufacturing of metals: a brief review of the characteristic microstructures and properties of steels, ti-6al-4v and high-entropy alloys," *Science and Technology of advanced MaTerialS*, vol. 18, no. 1, p. 584–610, 2017.

[23] A. E.-M. A. Mohamed, J. Zou, R. S. Sheridan, K. Bongs, and M. M. Attallah, "Magnetic shielding promotion via the control of magnetic anisotropy and thermal post processing in laser powder bed fusion processed nifemo-based soft magnet," *Additive Manufacturing*, vol. 32, p. 101079, 2020.

[24] G. Boussinot, M. Apel, J. Zielinski, U. Hecht, and J. H. Schleifenbaum, "Strongly out-of-equilibrium columnar solidification during laser powder-bed fusion in additive manufacturing," *Physical Review Applied*, vol. 11, no. 1, p. 014025, 2019.

[25] C.-K. Hou, "Effect of silicon on the loss separation and permeability of laminated steels," *Journal of magnetism and magnetic materials*, vol. 162, no. 2-3, p. 280–290, 1996.

[26] B. Zhang, Y. Li, and Q. Bai, "Defect formation mechanisms in selective laser melting: a review," *Chinese Journal of Mechanical Engineering*, vol. 30, no. 3, p. 515–527, 2017.

[27] M. Garibaldi, I. Ashcroft, N. Hillier, S. A. C. Harmon, and R. Hague, "Relationship between laser energy input, microstructures and magnetic properties of selective laser melted fe-6.9%wt si soft magnets," *Materials Characterization*, vol. 143, p. 144–151, 2018.

[28] C. Qiu, C. Panwisawas, M. Ward, H. C. Basoalto, J. W. Brooks, and M. M. Attallah, "On the role of melt flow into the surface structure and porosity

development during selective laser melting," *Acta Materialia*, vol. 96, p. 72–79, 2015.

[29] S. Gao, H. Liao, X. Yan, Q. Xie, C. Chang, B. Lu, X. Zhang, N. Fenineche, and M. Liu, "Magnetic and mechanical properties of additive manufactured fe-3wt.% si material," *Journal of Magnetism and Magnetic Materials*, vol. 580, p. 170907, 2023.

[30] S. Gao, *Additive manufacturing Processing and characterization of Fe-Si soft magnetic alloys*. Thesis, 2021.

[31] F. Liu, P. K. Liaw, and Y. Zhang, "Recent progress with bcc-structured high-entropy alloys," *Metals*, vol. 12, no. 3, p. 501, 2022.

DEPARTMENT OF INDUSTRIAL AND MATERIAL SCIENCE
CHALMERS UNIVERSITY OF TECHNOLOGY
Gothenburg, Sweden
www.chalmers.se

CHALMERS
UNIVERSITY OF TECHNOLOGY